Earth and Planetary Science Letters 617 (2023) 118261

Contents lists available at ScienceDirect

Earth and Planetary Science Letters

journal homepage: www.elsevier.com/locate/epsl

Sulfidation of nano-magnetite to pyrite: Implications for interpreting paleoenvironmental proxies and biosignature records in hydrothermal sulfide deposits

Eric A. Runge [a,b,*], Muammar Mansor [c], Jeremiah Shuster [d], Stefan Fischer [d], Yali Liu [e], Dominique J. Lunter [e], Andreas Kappler [c,f], Jan-Peter Duda [a,b,*]

[a] Sedimentology and Organic Geochemistry, Department of Geosciences, Tübingen University, Germany
[b] Geobiology, Geoscience Center, Göttingen University, Germany
[c] Geomicrobiology, Department of Geosciences, Tübingen University, Germany
[d] Tuebingen Structural Microscopy Core Facility, Tübingen University, Germany
[e] Pharmaceutical Technology, Department of Pharmacy and Biochemistry, Tübingen University, Germany
[f] Cluster of Excellence EXC 2124, Controlling Microbes to Fight Infection, Tübingen University, Germany

ARTICLE INFO

Article history:
Received 7 February 2023
Received in revised form 30 May 2023
Accepted 5 June 2023
Available online xxxx
Editor: L. Coogan

Keywords:
early life
emergence of life
sulfides
dissimilatory Fe(III)-reducing bacteria (DIRB)
magnetotactic bacteria (MTB)

ABSTRACT

Nano-magnetite is a potential archive for biosignatures and paleoenvironmental proxies in hydrothermal systems. However, sulfidic diagenesis at hydrothermal conditions potentially drives the rapid transformation of magnetite to Fe sulfide minerals. The identity and characteristics of transformation products from these reactions are crucial for interpreting biosignature records and paleoenvironmental proxies associated with Fe minerals in sulfide deposits. To constrain the preservation and transformation of magnetite in hydrothermal sulfide habitats, we incubated synthetic nano-magnetite in anoxic artificial seawater at a sulfide:Fe ratio of 4:1 as well as at different pH (7, 10) and temperatures (20-80 °C), and in presence or absence of added S^0. Experimental products were analyzed by means of sequential Fe extraction, μ-X-ray diffraction (μ-XRD), Raman spectroscopy, and scanning electron microscopy (SEM). After 46 days, nano-magnetite was only detected at 20 °C (pH ~10). Fe(III)-containing mackinawite and greigite formed at pH ~10 and ≥20 °C. At pH ~7 and 80 °C, magnetite was transformed to pyrite within only 19 days, with faster rates in the presence of polysulfides, which formed from the sulfide-mediated reduction of Fe(III) and in the presence of S^0. Our results demonstrate a potential taphonomic bias against nano-magnetite in sulfidic hydrothermal habitats and suggest that pyrite-associated paleoenvironmental proxies and biosignature records of Fe- and S-cycling microorganisms in hydrothermal deposits are affected by diagenetic fluid-mineral interactions.

1. Introduction

Nano-magnetite in natural environments forms via abiotic Fe(II)-catalyzed transformation of Fe(III) (oxyhydr)oxides or is driven by Fe-cycling microorganisms, such as dissimilatory Fe(III)-reducing bacteria (DIRB) or magnetotactic bacteria (MTB) (Amor et al., 2020; Hansel et al., 2005; Kirschvink and Chang, 1984). Abiotic and biogenic magnetite differ in morphology, crystallographic structure, magnetic properties, redox state, trace metal content, and stable isotopic fingerprints (e.g., Kirschvink and Chang, 1984; Thomas-Keprta et al., 2000; Carvallo et al., 2008; Lam et al., 2010; Amor et al., 2016, 2022; Han et al., 2021). Thus, nano-magnetite is a potential archive for biosignatures of Fe-cycling microorganisms. Moreover, the presence of nano-magnetite in sediments and rocks alongside its morphologic, geochemical, and isotopic characteristics has been used to infer past biological productivity, availability of nutrients and substrates, diagenetic redox conditions, climate change, ocean circulation and stratification, as well as paleomagnetic reconstructions (e.g., Chang et al., 2012; Havas et al., 2021; Hesse, 1994; Kopp and Kirschvink, 2008; Schumann et al., 2008; Yamazaki and Kawahata, 1998). However, these applications require a robust understanding of diagenetic processes affecting the preservation of nano-magnetite in different marine environments.

In marine sediments, both abiotic and biogenic magnetite are produced in anoxic to suboxic zones. These precipitates are typi-

* Corresponding authors at: Geobiology, Geoscience Center, Göttingen University, Germany.
E-mail addresses: eric.runge@uni-tuebingen.de (E.A. Runge), jan-peter.duda@uni-goettingen.de (J.-P. Duda).

https://doi.org/10.1016/j.epsl.2023.118261
0012-821X/

cally nm-sized and highly reactive due to their large relative surface area (Byrne et al., 2015; Hansel et al., 2005). This affects their preservation potential during sulfidic diagenesis driven by sulfur cycling microbes (SCM); while µm-sized sedimentary magnetite can be preserved for 1000s of years after burial in sulfidic zones (Canfield and Berner, 1987), experimentally synthesized nm-sized magnetite has a half-life of only 72 days at 1 mM dissolved sulfide, pH 7.5, and 25 °C (Poulton et al., 2004). Magnetite-producing MTB and DIRB are also widespread in hydrothermal sulfide systems (Roh et al., 2006; Sylvan et al., 2012). In these habitats, sulfide is not only supplied by SCM but also from fluids containing high concentrations of volcanogenic sulfide (Früh-Green et al., 2022). Elevated temperatures and high sulfide concentrations potentially drive the rapid sulfidation of magnetite in hydrothermal sulfide systems, which are among the most ancient microbial habitats on Earth (Van Kranendonk et al., 2008; Mißbach et al., 2021; Runge et al., 2022).

For hydrothermal sulfide deposits, the implications are twofold: biosignatures and environmental proxies associated with magnetite might be diagenetically altered or erased. On the other hand, the sulfidation of primary magnetite may yield distinct transformation products that might be subject for use as biosignatures and paleoenvironmental proxies themselves. Textural, trace element, and isotopic characteristics of pyrite, for example, are commonly used to trace microbial Fe- and S- cycling, fluid composition and temperature, as well as redox conditions in hydrothermal sulfide environments (e.g., Baumgartner et al., 2020; Li and Kusky, 2007; Nozaki et al., 2020; Ohmoto, 1972; Revan et al., 2014; Rouxel et al., 2004; Vearncombe et al., 1995). This highlights the importance of understanding the formation and diagenetic history of Fe sulfides in such habitats. Previous experiments on magnetite sulfidation were conducted at temperatures ≥125 °C (Bendt et al., 2019; Qian et al., 2013, 2010), excess Fe conditions (Nie et al., 2023), or excluded the characterization of transformation products (Poulton et al., 2004). Microbial activity and biogenic mineral formation, however, are limited to temperatures of ≤121 °C (Kashefi and Lovley, 2003), which occur along a mixing gradient from hot, acidic and sulfide-rich endmember fluids (~400 °C; pH 2-5) to seawater (2-4 °C; pH 8) in hydrothermal systems (Früh-Green et al., 2022). The stability of nano-magnetite and the identity and characteristics of its transformation products during in-situ sulfidation under conditions in such mixing zones have not been constrained so far.

Here, we simulate the sulfidic diagenesis of nano-magnetite in hydrothermal systems by incubating synthetic nanoparticles in anoxic artificial seawater at different sulfide:Fe ratios (4:1 and 1:4), pH (~7 and ~10), temperatures (20–80 °C), and in the presence or absence of added S^0, an important oxidant in pyrite forming reactions under anoxic conditions (Benning et al., 2000; Mansor and Fantle, 2019) that commonly co-occurs with Fe oxyhydr(oxides) in hydrothermal sulfide systems (Kelley et al., 2002). The results of our multi-analytical approach, combining sequential Fe extraction, μ-X-ray diffraction (μ-XRD), Raman spectroscopy, and the structural characterization of experimental products by scanning electron microscopy (SEM), demonstrate the rapid transformation of nano-magnetite to pyrite and suggest a strong in-situ taphonomic bias against primary magnetite preservation in hydrothermal sulfidic systems.

2. Materials and methods

2.1. Synthesis of magnetite nanoparticles

Magnetite nanoparticles were synthesized by dropwise titration of 100 mL anoxic solution containing 0.2 M $FeCl_3$: 0.1 M $FeCl_2$ in 0.3 M HCl with 100 g of anoxic 20% NaOH in a N_2-filled anoxic chamber while stirring at 600 rpm. The resulting suspension containing magnetite particles was further stirred at 600 rpm for 15 minutes. A magnet was placed against the bottle to hold the magnetic particles in place while the supernatant was removed and replaced by anoxic ultrapure H_2O (Milli-Q, Merck Millipore). This suspension was sonicated for 5 minutes and again replaced by anoxic ultrapure water. This washing procedure was repeated twice. The successful synthesis of the magnetite nanoparticles was confirmed using μ-X-ray diffraction (μ-XRD) (Fig. S1) and an average crystallite size of 12 nm was calculated based on XRD reflections using the Scherrer equation as detailed in (Mansor et al., 2019).

2.2. Experimental setups

The preparation of incubation experiments, sampling, and sample preparation for analysis were conducted in a N_2-filled chamber. Batch experiments were prepared in triplicate with total volumes of 50 mL in 100 mL-volume serum bottles closed with butyl stoppers to prevent the presence of oxygen. Artificial seawater was prepared using 17.30 g/L NaCl, 8.61 g/L $MgCl_2 \bullet 6H_2O$, 0.03 g/L $MgSO_4 \bullet 7H_2O$, 0.99 g/L $CaCl_2 \bullet 2H_2O$, 0.39 g/L KCl, 0.06 g/L KBr, 0.25 g/L NH_4Cl, and 1.85 g/L $NaHCO_3$. The pH of the resulting solution was adjusted to 7 using 0.5 mL of 1 M HCl, and dissolved O_2 was degassed by purging with 50/50 N_2/CO_2. An anoxic 1 M sulfide solution was made by dissolving Na_2S in O_2-free H_2O.

Batch experiments were prepared in triplicate with total volumes of 50 mL in 100 mL-volume serum bottles closed with butyl stoppers. The magnetite suspension and the sulfide solution were added to the artificial seawater at 60 mM sulfide and 15 mM Fe (4:1 molar ratio), representative of plausible hydrothermal fluids in modern black smoker environments (Hannington et al., 2005). This composition resulted in an initial pH of 10.3 that, during the experiment, remained constant at 20 and 40 °C, and slightly decreased to 9.2 and 9.5 at 60 and 80 °C, respectively (Fig. S2). Two additional setups were prepared that further contained (i) 200 mM MOPS buffer, and (ii) 200 mM MOPS buffer and 62 mM (100 mg) elemental sulfur (S^0, Sigma Aldrich, product # 13803), respectively. These experiments had a starting pH of 7.0, which slightly increased to 7.4 during the experiment (Fig. S2). The serum bottles for the pH ~10 experiments were incubated at 20, 40, 60, or 80 °C, and the pH ~7 experiments were incubated at 80 °C. Sampling for geochemical analysis was done after 0, 19, 30, or 46 days. For μ-XRD, Raman spectroscopy, and scanning electron microscopy (SEM), samples were taken after 19, 30, or 46 days.

2.3. Geochemical analyses

Aliquots (0.5 mL) of the mineral suspension were centrifuged for 5 minutes at 12,100 × g to separate the minerals from the "liquid" phase (this phase contains both the combined dissolved and colloidal Fe that did not settle during centrifugation). Fe concentrations in both fractions were quantified spectrophotometrically using the ferrozine assay (Stookey, 1970). Supernatants were acidified with 1 M HCl before analysis. Sequential Fe extraction of the solid phase using 6 M HCl (reactive Fe minerals: magnetite, mackinawite, and greigite) and 8 M HNO_3 (pyrite) was used to determine the extent of pyritization over time (Heron et al., 1994; Huerta-Diaz and Morse, 1990; Poulton and Canfield, 2005). Extraction with 6 M HCl was conducted for 24 hrs in an anoxic chamber in the presence of Ti(III)-citrate to prevent oxidation of dissolved sulfide to S^0, which could reduce Fe extraction yields (Rickard et al., 2006). Solid residues from the 6 M HCl extraction step were extracted with 8 M HNO_3 for >2 hrs. Polysulfides in the liquid phase were analyzed via UV-VIS spectroscopy in 1 mL plastic cuvettes using a spectral range of 250-500 nm.

2.4. μ-X-ray diffraction (μ-XRD)

Aliquots for μ-XRD measurements were taken in an N_2-filled anoxic chamber. Mineral pellets were harvested by centrifugation and washed three times with anoxic ultrapure water to remove residual salts before drying. Dry samples were stored in N_2-filled preserving jars until μ-XRD analysis under ambient atmospheric conditions (Boursiquot et al., 2001; Zhang et al., 2020). μ-XRD was performed on dry material using a Bruker's D8 Discover GADDS XRD^2 micro-diffractometer equipped with a standard sealed tube with a Co-anode (Co Kα radiation, $\lambda = 0.179$ nm) at 30 kV/30 mA. The total time measurement was 240 seconds at two detector positions (15° and 40°). Phase identification was validated using the Match! Software for phase identification from powder diffraction (Match!, Crystal Impact, Bonn, Germany, version 3.11.5.203) with the Crystallography Open Database (COD-Inorg REV211633 2018.19.25).

2.5. Raman spectroscopy

For Raman spectroscopy, aliquots from suspended samples were dried onto glass slides in an anoxic chamber. Glass slides were transported to the instrument in N_2-filled jars. Raman spectra were acquired with an Alpha 500R Confocal Raman Microscope (WITec GmbH, Ulm, Germany), which was equipped with a 532 nm excitation laser, an UHTS 300 spectrometer and a DV401-BV CCD camera. The optical grating was 600 g/mm for recording the spectra in the range of 0 to 3790 cm^{-1}. Herein, a 40× objective with a numerical aperture of 0.6 was used (EC Epiplan-neofluor, Carl Zeiss, Germany). The laser power was adjusted to 1 mW using an optical power meter (PM100D, Thorlabs GmbH, Dachau, Germany) to avoid excessive heating that potentially induces mineral transformation. Per sample, three spots were analyzed using 10 integrations for 10 to 20 seconds each. Spectra from these three spot measurements were combined into a composite spectrum, and relative intensities were normalized to 100. Magnetite and pyrite were identified using the software CrystalSleuth, the RRUFF database (https://rruff.info/; accessed 15 August 2022) and mackinawite (FeS_m) and greigite were compared to reference patterns from (Bourdoiseau et al., 2011, 2008).

2.6. Scanning electron microscopy (SEM)

For SEM analysis, samples were washed with anoxic Milli-Q water and dried onto carbon adhesive tabs attached to aluminium stubs in an anoxic chamber. The dried samples were coated with 8 nm of gold using a BAL-TEC SCD 005 sputter coater. The morphological characterization of the minerals was performed using a Crossbeam 550 L SEM (Zeiss, Oberkochen, Germany) operating at an acceleration voltage of 2 kV and working distances of 3.7 mm. All micrographs were taken using the Secondary Electron Secondary Ion (SESI) detector.

3. Results

3.1. Mineralogical analysis

After 46 days of incubation, magnetite was detected only at pH ~10 and 20 °C (Fig. 1). FeS_m was present in all experiments at pH ~10 (Fig. 1). The shifted band positions of FeS_m in our experiment (255 to 257 cm^{-1}and 315 to 317 cm^{-1}) relative to Fe(II)-mackinawite (208 and 282 cm^{-1}) indicates the presence of Fe(III) in the crystal structure (Bourdoiseau et al., 2008; Sanden et al., 2021). Greigite was only detected in experiments at pH ~10 and ≤40 °C after 46 days (Fig. 1), although it formed at 60 °C after 7 days (Fig. S3B). Pyrite was only detected after 46 days at pH ~7 (80 °C) in both the presence and absence of S^0 (Fig. 1).

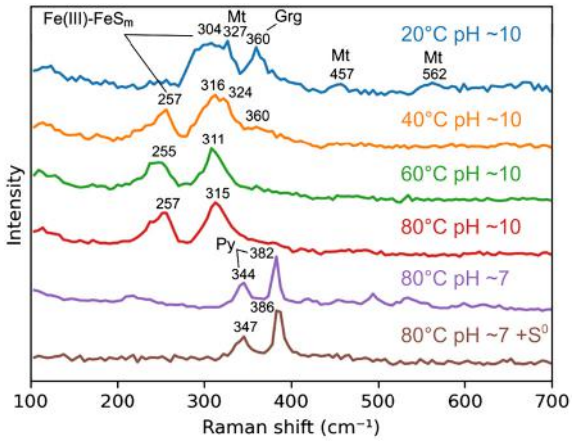

Fig. 1. Raman spectra of minerals from the incubation experiments after 46 days at a sulfide:Fe ratio of 4:1. Fe(III)-FeS_m: Fe(III)-containing mackinawite; Mt: magnetite; Grg: greigite; Py: pyrite.

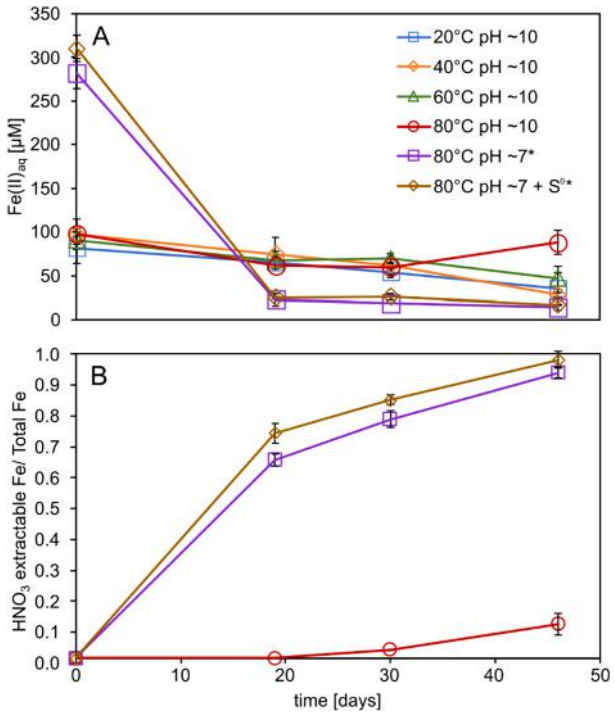

Fig. 2. Fe geochemistry of batch experiments. The error bars represent standard deviations of triplicate analysis. A: aqueous phase (combined dissolved and colloidal Fe); B: pyritization extent at a sulfide: Fe ratio of 4:1 as determined via sequential Fe extraction of the solid phase using 6 M HCl (magnetite/FeS_m/greigite) and 8 M HNO_3 (pyrite). *Denotes samples in which colloidal particles were not fully removed by centrifugation.

3.2. Geochemical analysis

In experiments at pH ~10, $Fe(II)_{aq}$ was generally low (≤100 μM) compared to the initial total Fe concentration (15 mM) and decreased slightly over time (Fig. 2B; Table S1). At 80 °C and pH ~10, the fraction of HNO_3 extractable Fe ($Fe[HNO_3/(HCl+HNO_3)]$) slightly increased to 0.1 over 46 days (Fig. 2B; Table S1), suggesting minor pyrite formation and/or cross-contamination from the 6 M HCl fraction. In experiments at pH ~7, $Fe(II)_{aq}$ was initially higher (~300 μM) compared to ones at pH ~10, and then dropped to ~24 μM within the first 19 days (Fig. 2B; Table S1). 6 M HCl extraction of the solid phase from these experiments after 19 days yielded black residues that were soluble in HNO_3, suggesting the presence of pyrite (Huerta-Diaz and Morse, 1990). The fraction of

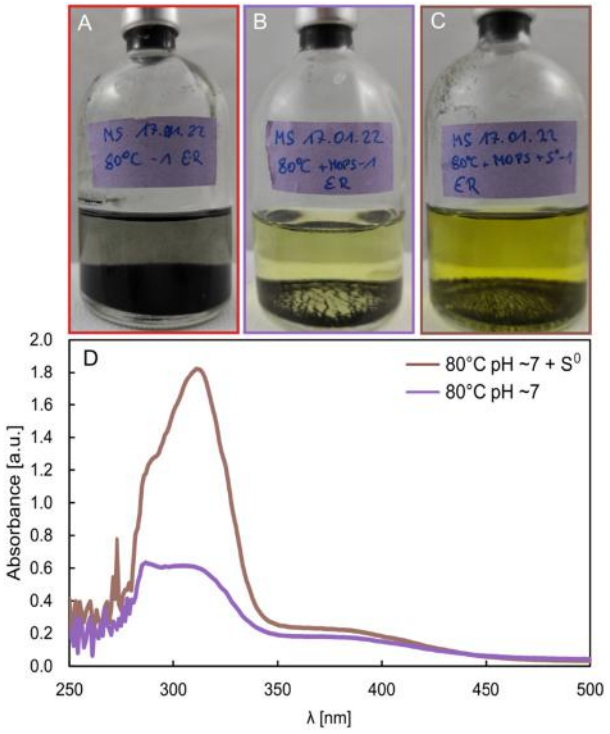

Fig. 3. Photographs of experimental bottles and UV-VIS spectra of dissolved polysulfides in experiments (80 °C, 19 days). No polysulfides were found in the experiments at pH ~10 (A). Polysulfides formation in experiments at pH ~7 was apparent from the yellow coloration (B, C). Note that the liquid in the experiment with added S^0 (C) has a more intense coloration than the experiment without added S^0 (B), indicating increased formation of polysulfides in the presence of added S^0. This is supported by a higher UV-VIS absorbance in the presence of S^0 (D). The difference in the peak position between both experiments at pH ~7 (D) may be due to variations in polysulfide chain-lengths.

HNO_3-extractable Fe (Fe[HNO_3/(HCl+HNO_3)]) at pH ~7 increased to ~1 within 46 days, indicating near-complete transformation of magnetite to pyrite with faster reaction rates in the presence of added S^0 (Fig. 2B). The yellowish coloring of the liquid phases and UV-VIS spectroscopy revealed that polysulfides formed in the experiments at pH ~7, but not at pH ~10 (Fig. 3).

3.3. SEM

Experiments at pH ~7 contained rosette-like structures comprised of tens of nm sized platy crystals (Fig. 4A-C) that are characteristic of FeS_m (Csákberényi-Malasics et al., 2012; Picard et al., 2018). Pyrite crystals in both experiments at pH ~7 were roughly bi-pyramidal in shape and ca. 2-5 µm in size (Fig. 4, e.g., D, I). All pyrite crystals from the experiment without additional S^0 exhibited poorly developed surfaces and had a dendritic habit (Fig. 4A-F). Dendritic pyrite also occurred in the presence of added S^0 but was much less prominent; instead, most pyrite crystals appeared more rounded with smoother crystal faces (Fig. 4G-L). Notably, pyrite crystals in experiments with added S^0 showed abundant nm-sized surface-bound globules of unknown composition (Fig. 4J-L). Over time, these globules increased in size from individual particles (after 19 days) to particle aggregates (after 30 d) (Fig. 4J-K). After 46 days, these aggregates were no longer present (Fig. 4L).

4. Discussion

4.1. Mineral (trans)formation

We suggest that the removal of magnetite from our experiments is driven by reductive dissolution in presence of excess sulfide (Eq. (1); Poulton et al., 2004). If this is the case, magnetite will dissolve at a much slower rate at excess Fe conditions. Therefore, we performed additional experiments with an equivalent setup to the pH ~10, 60 °C runs but varied the S:Fe ratio between 4 and 0.25. Raman spectroscopy of the resulting minerals demonstrates the presence of magnetite and absence of Fe sulfides after 7 days with excess Fe (Fig. S3A). At excess sulfide conditions, in contrast, magnetite signals are strongly diminished while Fe(III)-containing mackinawite (Fe(III)-FeS_m) and greigite are present (Fig. S3B). Therefore, we consider reductive dissolution by sulfide as the key-mechanism for the removal of magnetite from our experiments at excess sulfide conditions.

$$Fe_3O_4 + 4HS^- + 4H^+ \rightarrow 3FeS_m + 4H_2O + S^0 \quad (1)$$

At pH ~10, the formation of Fe(III)-FeS_m was most likely due to rapid reprecipitation after magnetite dissolution driven by excess sulfide (Eq. (1)). The incorporation of Fe(III) into the FeS_m structure may be due to a release of $Fe(III)_{aq}$ from magnetite during mineral dissolution, as previously observed during the reduction of sulfate green-rust [$Fe(II)_4Fe(III)_2(OH)_{12}SO_4 \bullet 8H_2O$] by sulfate-reducing bacteria (Langumier et al., 2009). Therefore, we suggest that the formation of Fe(III)-FeS_m at pH ~10 is the result of a dissolution-reprecipitation mechanism. The exclusive detection of greigite in experiments at pH ~10 and ≤40 °C after 46 days (Fig. 1) suggests a rate-dependent removal of greigite at higher temperatures, perhaps via reduction to FeS or transformation to pyrite.

At pH ~7, the high initial concentration of $Fe(II)_{aq}$ (Fig. 2A; Table S1) compared to pH ~10 experiments can be explained by the presence of dissolved or colloidal Fe(II), or both. It is unlikely that this difference is controlled by the solubility of FeS which is independent of pH above pH 6 (Rickard and Luther, 2007). However, it has been demonstrated that colloidal FeS precursors to crystalline FeS_m aggregate upon pH increase via oriented assembly, suggesting that the formation of FeS_m is promoted at higher pH (Matamoros-Veloza et al., 2018b, 2018a). We therefore attribute the higher initial concentration of $Fe(II)_{aq}$ at pH 7 mainly to the presence of colloidal FeS. The subsequent decrease of $Fe(II)_{aq}$ to ~25 μM after 19 days (pH ~7) (Fig. 2A; Table S1) is then most likely due to aggregation of colloidal FeS into FeS_m particles that are large enough to settle during centrifugation (Mirabello et al., 2020). We therefore suggest that the growth of initial Fe sulfides in pH ~7 experiments was driven by the assembly of colloidal FeS.

Pyrite can form via reaction of FeS_{aq} precursors with H_2S_{aq} ("H_2S pathway", Eq. (2); Rickard, 1997), surface-mediated sulfidation of Fe (oxyhydr)oxides (Ferric Hydroxide Surface "FHS pathway", Eq. (3)a-e; Peiffer et al., 2015), or oxidation of FeS_{aq} by dissolved polysulfides ("polysulfide pathway", Eq. (4), Rickard, 1975). Pyritization via the H_2S pathway is likely of minor importance in our experiments, due the limited abundance of $H_2S_{(aq)}$ from the speciation of $H_2S_{(aq)}/HS^-$ at pH 7 and the fact that the required reactions will be kinetically inhibited under strict anoxic conditions (Benning et al., 2000; Mansor and Fantle, 2019). The FHS pathway requires the presence of Fe (oxyhydr)oxide surfaces to proceed (Peiffer et al., 2015). However, at excess sulfide conditions, magnetite nanoparticles were mostly transformed to Fe sulfides within 7 days even at 60 °C (Fig. S3A). At the conditions in our pyrite-forming experiments (80 °C, excess sulfide) the removal of magnetite was likely even faster, while pyrite formation proceeded over 46 days (Fig. 2B). Therefore, the FHS pathway was most likely not quantitatively important in our experiments. In contrast, the higher abundance of polysulfides in the presence of added S^0 (Fig. 3) was associated with a faster pyritization rate (Fig. 2B), indicating a rate control of polysulfide availability on pyrite formation.

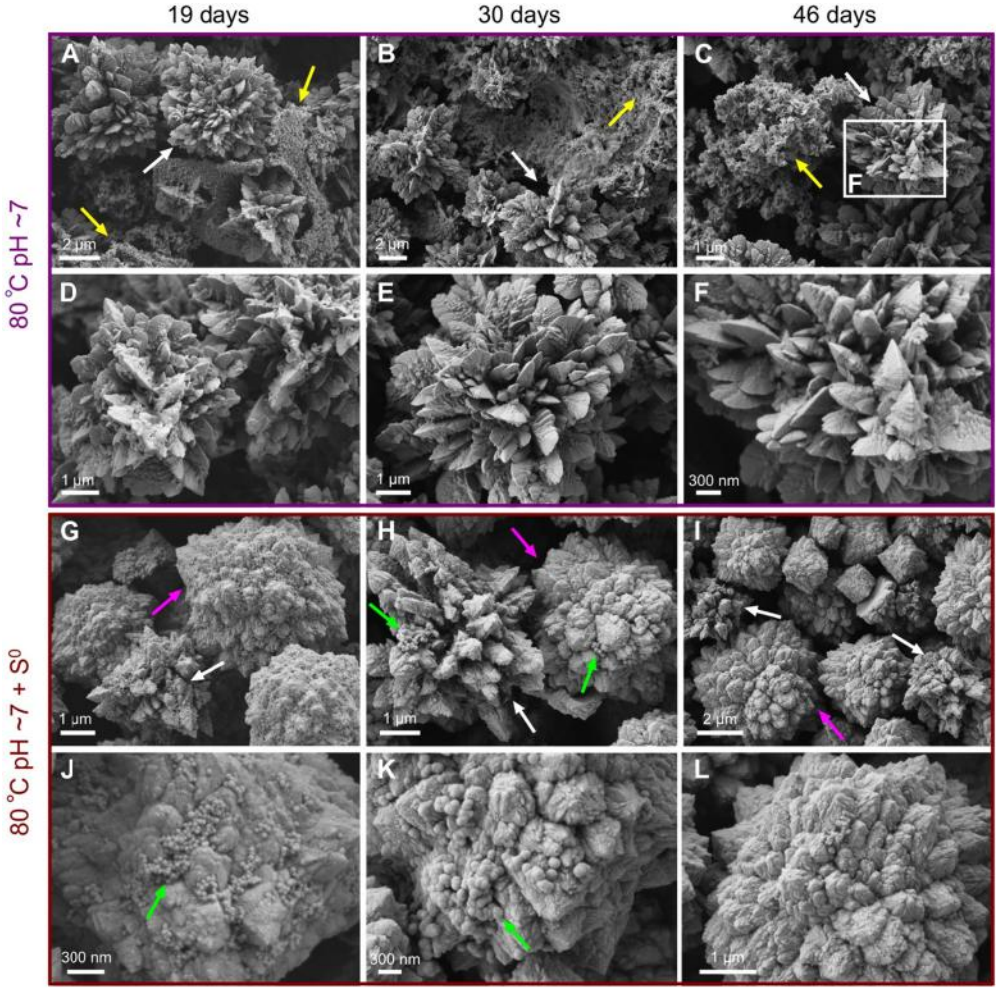

Fig. 4. SEM micrographs of samples taken throughout the incubation experiments at pH ~7. Pyrite crystals from experiments without added S^0 (purple frame) exclusively exhibited a distinct dendritic habit (A-F; white arrows) and were associated with platy nm-sized particles, likely FeS_m (A-C; yellow arrows). Note that this dendritic habit is still well-preserved after 46 days (F; white arrow). In contrast, most pyrite crystals in experiments without added S^0 (brown frame) appeared more rounded (G-L; pink arrows), although some dendritic pyrite crystals also occur in these experiments (G-I, white arrows). Pyrite crystals from this experiment also contained globular precipitates of unknown composition that were 100 s of nanometres in size (H, J-L; green arrows). These precipitates appeared to coalesce over time and become incorporated into pyrite crystals after 46 days (L).

For these reasons, we consider the polysulfide pathway the dominant pyrite formation mechanism in our experiments.

$$FeS_{aq} + H_2S \rightarrow FeS_2 + H_2 \quad (2)$$

$$> Fe^{III}OH + HS^- \leftrightarrow > Fe^{III}S^- + H_2O \quad (3a)$$

$$> Fe^{III}S^- \leftrightarrow > Fe^{II}S^{\bullet} \quad (3b)$$

$$> Fe^{II}S^{\bullet} + H_2O \leftrightarrow > Fe^{II}OH_2^+ + S^{\bullet -} \quad (3c)$$

$$> Fe^{II}OH_2^+ + 2S^{\bullet -} \rightarrow H_2O + > Fe^{II}S_2^- \quad (3d)$$

$$> Fe^{II}S_2^- \rightarrow FeS_{2,aq} + \text{new surface site} \quad (3e)$$

$$FeS_{aq} + S_2^{2-} \rightarrow FeS_2 + S^{2-} \quad (4)$$

4.2. Polysulfide formation

Polysulfide formation can occur via a reaction of HS^- or H_2S_{aq} with S^0 (Eq. (5); Rickard, 1975). This reaction is consistent with the more intense coloration of polysulfides in the experiment with added S^0 (Fig. 3) since sulfide was added in equal amounts to all experiments. However, polysulfides also formed at pH ~7 without added S^0, but not at pH ~10 (Fig. 3), suggesting polysulfide formation was also controlled by pH in addition to S^0 abundance. Eq. (5) predicts favorable conditions for polysulfide formation at higher pH, which is inconsistent with our observation (Fig. 3). Another possible pathway for polysulfide formation is the oxidation of HS^- on surfaces of Fe(III) mineral surfaces, which are more protonated at pH ~7 than at pH ~10, making surface-mediated oxidation of HS^- more efficient than in circumneutral solutions (Yao and Millero, 1996). Thus, oxidation of HS^- at the magnetite's surface led to formation of polysulfides as well as S^0, which in turn could promote even more polysulfide formation via the reaction between remaining HS^- and newly formed S^0 (Eq. (5)).

$$H_2S + S^0 \leftrightarrow S_2^{2-} + 2H^+ \quad (5)$$

4.3. Pyrite crystal growth

The exclusive presence of dendritic pyrite in experiments without added S^0 and the dominance of rounded pyrite in experiments with added S^0 (Fig. 4) suggests different particle growth mechanisms and/or reaction kinetics as a function of S^0 abundance. Dendritic pyrite is known from experimental synthesis and black smoker chimneys in the environment, and commonly used as indicator for formation temperatures $\leq$250 °C and rapid crystal growth at high degrees of supersaturation (Murowchick and

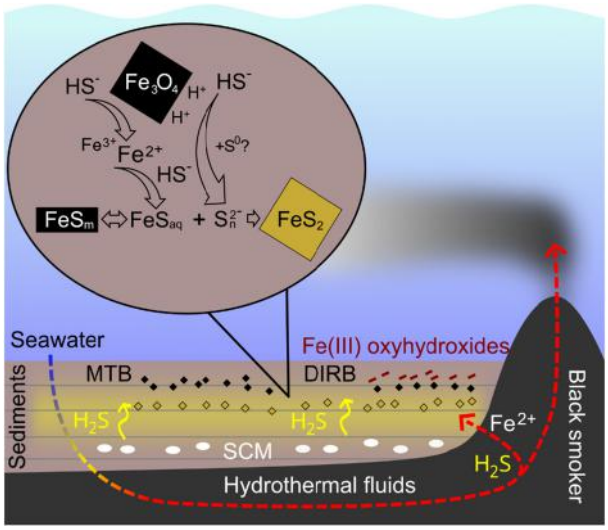

Fig. 5. Sulfidation of nano-magnetite to pyrite in a hydrothermal sulfide system. Nano-magnetite derives from MTB or reduction of Fe(III) oxyhydroxides by DIRB. During early diagenesis, volcanogenic and/or biogenic (from SCM) sulfide (H_2S/HS^-) in hydrothermal fluids causes reductive dissolution of magnetite in the sediment, yielding Fe^{2+} and minor Fe^{3+}. The reaction of Fe^{2+} and Fe^{3+} with HS^- leads to nucleation of Fe(III)-containing FeS_m. Polysulfides (S_n^{2-}) dominantly form via oxidation of HS^- during interaction with protonated magnetite surfaces and/or oxidation of HS^- by S^0. These polysulfides oxidize FeS_{aq} to pyrite (FeS_2).

Barnes, 1987; Wang et al., 2022). This suggests that the growth of dendritic pyrite in our experiments was fast, most likely driven by early surface-mediated polysulfide formation at pH ~7 and Fe_{aq} from rapidly dissolving magnetite at excess sulfide conditions. The presence of rounded pyrite crystals in experiments with S^0 (Fig. 4G-L) is consistent with expected reaction kinetics since S^0 facilitates the formation of polysulfides and thus pyrite (Berg et al., 2020; Rickard, 1975). Therefore, dendritic pyrite in both experiments might reflect the initial precipitation of approximately 2-5 µm-sized pyrite crystals. The presence of surface-associated globules on rounded pyrite crystals (Fig. 4J-L), in contrast, indicates a second stage of crystal growth proceeding at a faster rate in the presence of added S^0. Since magnetite surfaces were no longer available, polysulfides formed via Eq. (5) during this stage. The transformation of these globules from individual particles (after 19 days) to larger aggregates (after 30 days) indicates an assembly mechanism for their growth. After 46 days, these aggregates were no longer visible (Fig. 4L), suggesting their progressive incorporation into pyrite crystals. Thus, the growth of dendritic to rounded pyrite in the presence of added S^0 seems to proceed via attachment of nanocrystals followed by recrystallization (Gong et al., 2013). This mechanism seems to proceed without a visible increase in particle size (Fig. 4G-L), similar to skeletal growth (Salas et al., 2021).

4.4. Geological implications

A significant portion of magnetite in marine sediments is produced by DIRB and MTB (Amor et al., 2020; Kirschvink and Chang, 1984), which are widespread in hydrothermal systems (Roh et al., 2006; Sylvan et al., 2012) and might have emerged as early as in the Archean (Johnson et al., 2008; Lin et al., 2017). Indeed, syngenetic magnetite associated with organic matter is present in Earth's oldest hydrothermal sulfide deposits, that is, the ~3.2 Ga Sulphur Springs Group of Western Australia (Baumgartner et al., 2022). Hence, magnetite and its diagenetic transformation products might provide biosignature records in ancient hydrothermal sulfide systems, which are among the most ancient microbial habitats on Earth (Van Kranendonk et al., 2008; Mißbach et al., 2021; Runge et al., 2022). Our study demonstrates that nano-magnetite is rapidly transformed to Fe sulfides under conditions relevant to sulfidic hydrothermal habitats (Fig. 5), suggesting that any structural or geochemical information on paleoenvironmental conditions or microbial processes associated with nano-magnetite is rapidly erased or altered at hydrothermal temperatures as low as 80 °C. This likely results in a substantial taphonomic bias against authigenic Fe oxides in sulfidic hydrothermal systems throughout geological time.

Our results suggest that pyrite in hydrothermal deposits can be a secondary product from early diagenetic magnetite sulfidation (Fig. 5). The formation of dendritic pyrite in our experiments indicated rapid growth of initial pyrite crystals. In common marine sediments, sulfide is only supplied at a low rate by SCM, resulting in slow magnetite dissolution and a reduced supply of Fe_{aq} (cf. Canfield and Berner, 1987). In hydrothermal systems, however, magnetite sulfidation and dendritic pyrite formation may be driven by abundant sulfide from both biogenic and volcanogenic sources (Früh-Green et al., 2022), causing rapid magnetite dissolution. This implies that morphological, trace element, and isotopic characteristics of some pyrites in sulfide deposits may not record primary signals but be the result of a diagenetic interaction of a magnetite precursor with hydrothermal fluids. Moreover, the observed pyrite growth mechanisms in presence of added S^0 would produce zoned crystals (Salas et al., 2021), which may record geochemical and isotopic signals from multiple growth stages and, hence, time-averaged signals in bulk analysis. Thus, our study highlights the importance of a detailed understanding of diagenetic mineral (trans)formation for interpreting paleoenvironmental and biosignature records of Fe- and S-cycling microorganisms in hydrothermal sulfides.

5. Conclusions

We experimentally demonstrated the rapid sulfidation of nano-magnetite to pyrite under conditions similar to those prevailing in sulfidic hydrothermal habitats. The transformation of magnetite to pyrite occurred within 19 days (80 °C, pH ~7) and was faster in the presence of added S^0. This transformation proceeds via a multistep process, involving (i) reductive dissolution of magnetite by aqueous sulfide, (ii) reprecipitation of Fe(III)-containing FeS_m, (iii) transformation of Fe(III)-FeS_m to pyrite via the polysulfide pathway, and (iv) pyrite growth via particle attachment. Our findings strongly suggest that sulfidic diagenesis of nano-magnetite in hydrothermal habitats drives pyrite formation, likely resulting in a substantial preservation bias against authigenic magnetite in hydrothermal sulfide systems. Thus, magnetite sulfidation is an important process to consider when interpreting paleoenvironmental proxies and biosignatures of Fe- and S-cycling microorganisms in hydrothermal deposits throughout geological time.

CRediT authorship contribution statement

Eric A. Runge: Conceptualization, Data curation, Formal analysis, Investigation, Methodology, Validation, Visualization, Writing – original draft, Writing – review & editing. **Muammar Mansor:** Conceptualization, Funding acquisition, Methodology, Supervision, Validation, Writing – review & editing. **Jeremiah Shuster:** Formal analysis, Writing – review & editing. **Stefan Fischer:** Funding acquisition, Writing – review & editing. **Yali Liu:** Formal analysis, Software. **Dominique J. Lunter:** Formal analysis, Software. **Andreas Kappler:** Conceptualization, Funding acquisition, Methodology, Supervision, Validation, Writing – review & editing. **Jan-Peter Duda:** Conceptualization, Funding acquisition, Methodology, Supervision, Validation, Writing – review & editing.

Declaration of competing interest

The authors declare that they have no known competing financial interests or personal relationships that could have appeared to influence the work reported in this paper.

Data availability

Data will be made available on request.

Acknowledgements

This study was supported by the DFG (SPP 1833, Emmy Noether Programme; DU 1450/3-2, DU 1450/7-1; JPD, ER; INST 37/1027-1 FUGG; AK) as well as by the German Excellence Strategy of the German Federal and State Governments (EXC2124, 390838134; Tübingen Structural Microscopy Core Facility; AK, MM, SF, JS).

Appendix A. Supplementary material

Supplementary material related to this article can be found online at https://doi.org/10.1016/j.epsl.2023.118261.

References

Amor, M., Busigny, V., Louvat, P., Gélabert, A., Cartigny, P., Durand-Dubief, M., Ona-Nguema, G., Alphandéry, E., Chebbi, I., Guyot, F., 2016. Mass-dependent and -independent signature of Fe isotopes in magnetotactic bacteria. Science 352, 705–708. https://doi.org/10.1126/science.aad7632.

Amor, M., Tharaud, M., Gélabert, A., Komeili, A., 2020. Single-cell determination of iron content in magnetotactic bacteria: implications for the iron biogeochemical cycle. Environ. Microbiol. 22, 823–831. https://doi.org/10.1111/1462-2920.14708.

Amor, M., Wan, J., Egli, R., Carlut, J., Gatel, C., Andersen, I.M., Snoeck, E., Komeili, A., 2022. Key signatures of magnetofossils elucidated by mutant magnetotactic bacteria and micromagnetic calculations. J. Geophys. Res., Solid Earth 127, e2021JB023239. https://doi.org/10.1029/2021JB023239.

Baumgartner, R.J., Teece, B.L., Rasmussen, B., Muhling, J., Rickard, W.D.A., Pejcic, B., Hu, S., Bourdet, J., Caruso, S., Van Kranendonk, M.J., Grice, K., 2022. Exceptional preservation of organic matter and iron-organic colloidal mineralization in hydrothermal black smoker-type sulfide mineralization from the Paleoarchean seafloor. Chem. Geol., 121296. https://doi.org/10.1016/j.chemgeo.2022.121296.

Baumgartner, R.J., Van Kranendonk, M.J., Pagès, A., Fiorentini, M.L., Wacey, D., Ryan, C., 2020. Accumulation of transition metals and metalloids in sulfidized stromatolites of the 3.48 billion–year–old Dresser Formation, Pilbara Craton. Precambrian Res. 337, 105534. https://doi.org/10.1016/j.precamres.2019.105534.

Bendt, G., Saddeler, S., Schulz, S., 2019. Sulfidation of magnetite nanoparticles – following the polysulfide pathway. Eur. J. Inorg. Chem., 602–608.

Benning, L.G., Wilkin, R.T., Barnes, H.L., 2000. Reaction pathways in the Fe–S system below 100 °C. Chem. Geol. 167, 25–51. https://doi.org/10.1016/S0009-2541(99)00198-9.

Berg, J.S., Duverger, A., Cordier, L., Laberty-Robert, C., Guyot, F., Miot, J., 2020. Rapid pyritization in the presence of a sulfur/sulfate-reducing bacterial consortium. Sci. Rep. 10, 8264. https://doi.org/10.1038/s41598-020-64990-6.

Bourdoiseau, J.-A., Jeannin, M., Rémazeilles, C., Sabot, R., Refait, P., 2011. The transformation of mackinawite into greigite studied by Raman spectroscopy: transformation of mackinawite into greigite. J. Raman Spectrosc. 42, 496–504. https://doi.org/10.1002/jrs.2729.

Bourdoiseau, J.-A., Jeannin, M., Sabot, R., Rémazeilles, C., Refait, Ph., 2008. Characterisation of mackinawite by Raman spectroscopy: effects of crystallisation, drying and oxidation. Corros. Sci. 50, 3247–3255. https://doi.org/10.1016/j.corsci.2008.08.041.

Boursiquot, S., Mullet, M., Abdelmoula, M., Génin, J.-M., Ehrhardt, J.-J., 2001. The dry oxidation of tetragonal FeS_{1-x} mackinawite. Phys. Chem. Miner. 28, 600–611. https://doi.org/10.1007/s002690100193.

Byrne, J.M., Muhamadali, H., Coker, V.S., Cooper, J., Lloyd, J.R., 2015. Scale-up of the production of highly reactive biogenic magnetite nanoparticles using Geobacter sulfurreducens. J. R. Soc. Interface 12, 20150240. https://doi.org/10.1098/rsif.2015.0240.

Canfield, D.E., Berner, R.A., 1987. Dissolution and pyritization of magnetite in anoxic marine sediments. Deep Sea Research Part B. Oceanogr. Lit. Rev. 51, 645–659. https://doi.org/10.1016/0198-0254(87)90182-8.

Carvallo, C., Sainctavit, P., Arrio, M.-A., Menguy, N., Wang, Y., Ona-Nguema, G., Brice-Profeta, S., 2008. Biogenic vs. abiogenic magnetite nanoparticles: a XMCD study. Am. Mineral. 93, 880–885. https://doi.org/10.2138/am.2008.2713.

Chang, L., Roberts, A.P., Williams, W., Fitz Gerald, J.D., Larrasoaña, J.C., Jovane, L., Muxworthy, A.R., 2012. Giant magnetofossils and hyperthermal events. Earth Planet. Sci. Lett. 351–352, 258–269. https://doi.org/10.1016/j.epsl.2012.07.031.

Csákberényi-Malasics, D., Rodriguez-Blanco, J.D., Kis, V.K., Rečnik, A., Benning, L.G., Pósfai, M., 2012. Structural properties and transformations of precipitated FeS. Chem. Geol. 294–295, 249–258. https://doi.org/10.1016/j.chemgeo.2011.12.009.

Früh-Green, G.L., Kelley, D.S., Lilley, M.D., Cannat, M., Chavagnac, V., Baross, J.A., 2022. Diversity of magmatism, hydrothermal processes and microbial interactions at mid-ocean ridges. Nat. Rev. Earth Environ 3, 852–871. https://doi.org/10.1038/s43017-022-00364-y.

Gong, M., Kirkeminde, A., Ren, S., 2013. Symmetry-defying iron pyrite (FeS_2) nanocrystals through oriented attachment. Sci. Rep. 3, 2092. https://doi.org/10.1038/srep02092.

Han, X., Tomaszewski, E.J., Schoenberg, R., Konhauser, K.O., Amor, M., Pan, Y., Warter, V., Kappler, A., Byrne, J.M., 2021. Using Zn and Ni behavior during magnetite precipitation in banded iron formations to determine its biological or abiotic origin. Earth Planet. Sci. Lett. 568, 117052. https://doi.org/10.1016/j.epsl.2021.117052.

Hannington, M.D., De Ronde, C.E.J., Petersen, S., 2005. Sea-floor tectonics and submarine hydrothermal systems. In: Economic Geology 100th Anniversary Volume, pp. 111–141.

Hansel, C.M., Benner, S.G., Fendorf, S., 2005. Competing Fe(II)-induced mineralization pathways of Ferrihydrite. Environ. Sci. Technol. 39, 7147–7153. https://doi.org/10.1021/es050666z.

Havas, R., Savian, J.F., Busigny, V., 2021. Iron isotope signature of magnetofossils and oceanic biogeochemical changes through the Middle Eocene Climatic Optimum. Geochim. Cosmochim. Acta 311, 332–352. https://doi.org/10.1016/j.gca.2021.07.007.

Heron, Gorm, Crouzet, Catherine, Bourg, A.C.M., Christensen, T.H., 1994. Speciation of Fe(II) and Fe(III) in contaminated aquifer sediments using chemical extraction techniques. Environ. Sci. Technol. 28, 1698–1705. https://doi.org/10.1021/es00058a023.

Hesse, P.P., 1994. Evidence for bacterial palaeoecological origin of mineral magnetic cycles in oxic and sub-oxic Tasman Sea sediments. Mar. Geol. 117, 1–17. https://doi.org/10.1016/0025-3227(94)90003-5.

Huerta-Diaz, M.A., Morse, J.W., 1990. A quantitative method for determination of trace metal concentrations in sedimentary pyrite. Mar. Chem. 29, 119–144.

Johnson, C.M., Beard, B.L., Roden, E.E., 2008. The iron isotope fingerprints of redox and biogeochemical cycling in modern and ancient Earth. Annu. Rev. Earth Planet. Sci. 36, 457–493. https://doi.org/10.1146/annurev.earth.36.031207.124139.

Kashefi, K., Lovley, D.R., 2003. Extending the upper temperature limit for life. Science 301, 934. https://doi.org/10.1126/science.1086823.

Kelley, D.S., Baross, J.A., Delaney, J.R., 2002. Volcanoes, fluids, and life at mid-ocean ridge spreading centers. Annu. Rev. Earth Planet. Sci. 30, 385–491. https://doi.org/10.1146/annurev.earth.30.091201.141331.

Kirschvink, J.L., Chang, S.-B.R., 1984. Ultrafine-grained magnetite in deep-sea sediments: possible bacterial magnetofossils. Geology 12, 559–562.

Kopp, R.E., Kirschvink, J.L., 2008. The identification and biogeochemical interpretation of fossil magnetotactic bacteria. Earth-Sci. Rev. 86, 42–61. https://doi.org/10.1016/j.earscirev.2007.08.001.

Lam, K.P., Hitchcock, A.P., Obst, M., Lawrence, J.R., Swerhone, G.D.W., Leppard, G.G., Tyliszczak, T., Karunakaran, C., Wang, J., Kaznatcheev, K., Bazylinski, D.A., Lins, U., 2010. Characterizing magnetism of individual magnetosomes by X-ray magnetic circular dichroism in a scanning transmission X-ray microscope. Chem. Geol. 270, 110–116. https://doi.org/10.1016/j.chemgeo.2009.11.009.

Langumier, M., Sabot, R., Obame-Ndong, R., Jeannin, M., Sablé, S., Refait, Ph., 2009. Formation of Fe(III)-containing mackinawite from hydroxysulphate green rust by sulphate reducing bacteria. Corros. Sci. 51, 2694–2702. https://doi.org/10.1016/j.corsci.2009.07.001.

Li, J., Kusky, T.M., 2007. World's largest known Precambrian fossil black smoker chimneys and associated microbial vent communities, North China: implications for early life. Gondwana Res. 12, 84–100. https://doi.org/10.1016/j.gr.2006.10.024.

Lin, W., Paterson, G.A., Zhu, Q., Wang, Y., Kopylova, E., Li, Y., Knight, R., Bazylinski, D.A., Zhu, R., Kirschvink, J.L., Pan, Y., 2017. Origin of microbial biomineralization and magnetotaxis during the Archean. Proc. Natl. Acad. Sci. USA 114, 2171–2176. https://doi.org/10.1073/pnas.1614654114.

Mansor, M., Berti, D., Hochella, M.F., Murayama, M., Xu, J., 2019. Phase, morphology, elemental composition, and formation mechanisms of biogenic and abiogenic Fe-Cu-sulfide nanoparticles: a comparative study on their occurrences under anoxic conditions. Am. Mineral. 104, 703–717. https://doi.org/10.2138/am-2019-6848.

Mansor, M., Fantle, M.S., 2019. A novel framework for interpreting pyrite-based Fe isotope records of the past. Geochim. Cosmochim. Acta 253, 39–62. https://doi.org/10.1016/j.gca.2019.03.017.

Matamoros-Veloza, A., Cespedes, O., Johnson, B.R.G., Stawski, T.M., Terranova, U., de Leeuw, N.H., Benning, L.G., 2018a. A highly reactive precursor in the iron sulfide system. Nat. Commun. 9, 3125. https://doi.org/10.1038/s41467-018-05493-x.

Matamoros-Veloza, A., Stawski, T.M., Benning, L.G., 2018b. Nanoparticle assembly leads to mackinawite formation. Cryst. Growth Des. 18, 6757–6764. https://doi.org/10.1021/acs.cgd.8b01025.

Mirabello, G., Ianiro, A., Bomans, P.H.H., Yoda, T., Arakaki, A., Friedrich, H., de With, G., Sommerdijk, N.A.J.M., 2020. Crystallization by particle attachment is a colloidal assembly process. Nat. Mater. 19, 391–396. https://doi.org/10.1038/s41563-019-0511-4.

Mißbach, H., Duda, J.-P., van den Kerkhof, A.M., Lüders, V., Pack, A., Reitner, J., Thiel, V., 2021. Ingredients for microbial life preserved in 3.5 billion-year-old fluid inclusions. Nat. Commun. 12, 1101. https://doi.org/10.1038/s41467-021-21323-z.

Murowchick, J.B., Barnes, H.L., 1987. Effects of temperature and degree of supersaturation on pyrite morphology. Am. Mineral. 72, 1241–1250.

Nie, M., Li, X., Ding, Y., Pan, Y., Cai, Y., Liu, Y., Liu, J., 2023. Effect of stoichiometry on nanomagnetite sulfidation. Environ. Sci. Technol. 57 (1), 3002–3011. https://doi.org/10.1021/acs.est.2c08179.

Nozaki, T., Nagase, T., Ushikubo, T., Shimizu, K., Ishibashi, J., the D/V Chikyu Expedition 909 Scientists, 2020. Microbial sulfate reduction plays an important role at the initial stage of subseafloor sulfide mineralization. Geology 49, 222–227. https://doi.org/10.1130/G47943.1.

Ohmoto, H., 1972. Systematics of sulfur and carbon isotopes in hydrothermal ore deposits. Econ. Geol. 67, 551–578.

Peiffer, S., Behrends, T., Hellige, K., Larese-Casanova, P., Wan, M., Pollok, K., 2015. Pyrite formation and mineral transformation pathways upon sulfidation of ferric hydroxides depend on mineral type and sulfide concentration. Chem. Geol. 400, 44–55. https://doi.org/10.1016/j.chemgeo.2015.01.023.

Picard, A., Gartman, A., Clarke, D.R., Girguis, P.R., 2018. Sulfate-reducing bacteria influence the nucleation and growth of mackinawite and greigite. Geochim. Cosmochim. Acta 220, 367–384. https://doi.org/10.1016/j.gca.2017.10.006.

Poulton, S.W., Canfield, D.E., 2005. Development of a sequential extraction procedure for iron: implications for iron partitioning in continentally derived particulates. Chem. Geol. 214, 209–221. https://doi.org/10.1016/j.chemgeo.2004.09.003.

Poulton, S.W., Krom, M.D., Raiswell, R., 2004. A revised scheme for the reactivity of iron (oxyhydr)oxide minerals towards dissolved sulfide. Geochim. Cosmochim. Acta 68, 3703–3715. https://doi.org/10.1016/j.gca.2004.03.012.

Qian, G., Brugger, J., Skinner, W.M., Chen, G., Pring, A., 2010. An experimental study of the mechanism of the replacement of magnetite by pyrite up to 300 °C. Geochim. Cosmochim. Acta 74, 5610–5630. https://doi.org/10.1016/j.gca.2010.06.035.

Qian, G., Brugger, J., Testemale, D., Skinner, W., Pring, A., 2013. Formation of As(II)-pyrite during experimental replacement of magnetite under hydrothermal conditions. Geochim. Cosmochim. Acta 100, 1–10. https://doi.org/10.1016/j.gca.2012.09.034.

Revan, M.K., Genç, Y., Maslennikov, V.V., Maslennikova, S.P., Large, R.R., Danyushevsky, L.V., 2014. Mineralogy and trace-element geochemistry of sulfide minerals in hydrothermal chimneys from the Upper-Cretaceous VMS deposits of the eastern Pontide orogenic belt (NE Turkey). Ore Geol. Rev. 63, 129–149. https://doi.org/10.1016/j.oregeorev.2014.05.006.

Rickard, D., 1997. Kinetics of pyrite formation by the H2S oxidation of iron (II) monosulfide in aqueous solutions between 25 and 125 °C: the rate equation. Geochim. Cosmochim. Acta 61, 115–134. https://doi.org/10.1016/S0016-7037(96)00321-3.

Rickard, D., Griffith, A., Oldroyd, A., Butler, I.B., Lopez-Capel, E., Manning, D.A.C., Apperley, D.C., 2006. The composition of nanoparticulate mackinawite, tetragonal iron(II) monosulfide. Chem. Geol. 235, 286–298. https://doi.org/10.1016/j.chemgeo.2006.07.004.

Rickard, D., Luther, G.W., 2007. Chemistry of iron sulfides. Chem. Rev. 107, 514–562. https://doi.org/10.1021/cr0503658.

Rickard, D.T., 1975. Kinetics and mechanism of pyrite formation at low temperatures. Am. J. Sci. 275, 636–652.

Roh, Y., Gao, H., Vali, H., Kennedy, D.W., Yang, Z.K., Gao, W., Dohnalkova, A.C., Stapleton, R.D., Moon, J.-W., Phelps, T.J., Fredrickson, J.K., Zhou, J., 2006. Metal reduction and iron biomineralization by a psychrotolerant Fe(III)-reducing bacterium, *Shewanella* sp. Strain PV-4. Appl. Environ. Microbiol. 72, 3236–3244. https://doi.org/10.1128/AEM.72.5.3236-3244.2006.

Rouxel, O., Fouquet, Y., Ludden, J.N., 2004. Subsurface processes at the lucky strike hydrothermal field, Mid-Atlantic ridge: evidence from sulfur, selenium, and iron isotopes. Geochim. Cosmochim. Acta 68, 2295–2311. https://doi.org/10.1016/j.gca.2003.11.029.

Runge, E.A., Mansor, M., Kappler, A., Duda, J.-P., 2022. Microbial biosignatures in ancient hydrothermal sulfides. Geobiology, 12539. https://doi.org/10.1111/gbi.12539.

Salas, P., Ruprecht, P., Hernández, L., Rabbia, O., 2021. Out-of-sequence skeletal growth causing oscillatory zoning in arc olivines. Nat. Commun. 12, 4069. https://doi.org/10.1038/s41467-021-24275-6.

Sanden, S.A., Szilagyi, R.K., Li, Y., Kitadai, N., Webb, S.M., Yano, T., Nakamura, R., Hara, M., McGlynn, S.E., 2021. Electrochemically induced metal- *vs.* ligand-based redox changes in mackinawite: identification of a Fe^{3+} - and polysulfide-containing intermediate. Dalton Trans. 50, 11763–11774. https://doi.org/10.1039/D1DT01684A.

Schumann, D., Raub, T.D., Kopp, R.E., Guerquin-Kern, J.-L., Wu, T.-D., Rouiller, I., Smirnov, A.V., Sears, S.K., Lücken, U., Tikoo, S.M., Hesse, R., Kirschvink, J.L., Vali, H., 2008. Gigantism in unique biogenic magnetite at the Paleocene–Eocene thermal maximum. Proc. Natl. Acad. Sci. USA 105, 17648–17653. https://doi.org/10.1073/pnas.0803634105.

Stookey, L.L., 1970. Ferrozine - a new spectrophotometric feagent for iron. Anal. Chem. 42, 779–781. https://doi.org/10.1021/ac60289a016.

Sylvan, J.B., Toner, B.M., Edwards, K.J., 2012. Life and death of deep-sea vents: bacterial diversity and ecosystem succession on inactive hydrothermal sulfides. mBio 3, e00279-11. https://doi.org/10.1128/mBio.00279-11.

Thomas-Keprta, K.L., Bazylinski, D.A., Kirschvink, J.L., Clemett, S.J., Mckay, D.S., Wentworth, S.J., Vali, H., Jr, E.K.G., Romanek, C.S., 2000. Elongated prismatic magnetite crystals in ALH84001 carbonate globules: potential Martian magnetofossils. Geochim. Cosmochim. Acta 64, 4049–4081.

Van Kranendonk, M., Philippot, P., Lepot, K., Bodorkos, S., Pirajno, F., 2008. Geological setting of Earth's oldest fossils in the ca. 3.5 Ga dresser formation, Pilbara Craton Western Australia. Precambrian Res. 167, 93–124. https://doi.org/10.1016/j.precamres.2008.07.003.

Vearncombe, S., Barley, M.E., Groves, D.I., McNaughton, N.J., Mikucki, E.J., Vearncombe, J.R., 1995. 3.26 Ga black smoker-type mineralization in the Strelley Belt, Pilbara Craton, Western Australia. J. Geol. Soc. 152, 587–590. https://doi.org/10.1144/gsjgs.152.4.0587.

Wang, S., Li, C., Li, B., Dang, Y., Ye, J., Zhu, Z., Zhang, L., Shi, X., 2022. Constraints on fluid evolution and growth processes of black smoker chimneys by pyrite geochemistry: a case study of the Tongguan hydrothermal field, South Mid-Atlantic Ridge. Ore Geol. Rev. 140, 104410. https://doi.org/10.1016/j.oregeorev.2021.104410.

Yamazaki, T., Kawahata, H., 1998. Organic carbon flux controls the morphology of magnetofossils in marine sediments. Geology 26, 1064–1066. https://doi.org/10.1130/0091-7613(1998)026<1064:OCFCTM>2.3.CO;2.

Yao, W., Millero, F.J., 1996. Oxidation of hydrogen sulfide by hydrous Fe(III) oxides in seawater. Mar. Chem. 52, 1–16. https://doi.org/10.1016/0304-4203(95)00072-0.

Zhang, Q., Appel, E., Stanjek, H., Byrne, J.M., Berthold, C., Sorwat, J., Rösler, W., Seemann, T., 2020. Humidity related magnetite alteration in an experimental setup. Geophys. J. Int. 224, 69–85. https://doi.org/10.1093/gji/ggaa394.